Origin of spin-polarized hybrid states in epitaxial and rotated graphene on cobalt

https://doi.org/10.1016/j.carbon.2022.07.011

Matteo Jugovac,[*,†,‡,¶] Edward Donkor,[§,‖] Paolo Moras,[‡] Iulia Cojocariu,[†] Francesca Genuzio,[¶] Giovanni Zamborlini,[†] Giovanni Di Santo,[¶] Luca Petaccia,[¶] Natasa Stojic,[§,‖] Vitaliy Feyer,[†,⊥] Claus Michael Schneider,[†,⊥] Andrea Locatelli,[¶] and Tevfik Onur Menteş[*,¶]

†*Peter Grünberg Institute (PGI-6), Forschungszentrum Jülich GmbH, 52425 Jülich, Germany*

‡*Istituto di Struttura della Materia-CNR (ISM-CNR), Trieste, 34149, Italy*

¶*Elettra Sincrotrone Trieste, S.S. 14 km 163.5 in AREA Science Park, Basovizza, 34149 Trieste, Italy*

§*Abdus Salam International Centre for Theoretical Physics, 34151 Trieste, Italy*

‖*IOM-CNR Democritos, 34151 Trieste, Italy*

⊥*Fakultät f. Physik and Center for Nanointegration Duisburg-Essen (CENIDE), Universität Duisburg-Essen, 47048 Duisburg, Germany*

E-mail: matteo.jugovac@elettra.eu; tevfik.mentes@elettra.eu

Abstract

It is known that at the epitaxially-aligned graphene/Co(0001) interface a weakly-dispersing single spin conical band feature is found in the proximity of the Fermi level at the $\overline{\mathrm{K}}$ point in the surface Brillouin zone. Here, we experimentally and theoretically demonstrate that a similar band feature forms also in the case of rotated graphene domains on Co(0001). Spin-resolved reciprocal space maps show that the band feature in rotated graphene has similar Fermi velocity and spin polarization as its counterpart in epitaxially-aligned graphene. Density-functional-theory simulations carried out for the experimentally observed graphene orientations, reproduce the highly spin-polarized conical band feature at the graphene $\overline{\mathrm{K}}$ point, characterized by a hybrid π-d orbital character. The presence of the conical features in the rotated domains is attributed to the unfolding of the superstructure $\overline{\mathrm{K}}$ point states exclusively to the $\overline{\mathrm{K}}$ point of the graphene primitive cell. The similarities found in the electronic character for different graphene orientations are crucial in understanding the magnetic properties of realistic graphene/Co interfaces, facilitating the implementation in spintronics applications.

Keywords: graphene, cobalt, rotated, CVD, spin.

Introduction

The aim of spintronics is to utilize the spin in addition to electron charge as information carrier allowing to develop high-speed devices with low-power consumption.[1] For this purpose, the possibility and boundary conditions of spin injection, transport, and detection have been demonstrated in several model systems.[2–4] Recently, graphene with intrinsically high carrier mobility, small spin-orbit coupling, gate tunability and large spin diffusion length at room temperature, has been proposed as a building block for the realization of novel spintronic devices.[5–8] Towards this goal, spin polarization in graphene has been induced by doping, controlling defects and, most importantly, by coupling it to a ferromagnetic material.[9–13]

Among ferromagnetic support materials for graphene, cobalt has attracted the largest attention due to the structural matching and the electronic interaction between the two. Contacting graphene with cobalt was shown to result in a range of phenomena spanning from efficient spin injection,[14] spin reorientation in thin cobalt films[15] and the presence of a Rashba-type Dzyaloshinskii-Moriya interaction (DMI) at the graphene-cobalt interface.[16–18] At the basis of these interactions lies the orbital hybridization at the interface, which results in a spin polarized state near the Fermi level, termed as *minicone* by Usachov *et al.*.[19]

Based on the good structural matching between cobalt and graphene,[20] most studies on the electronic structure of the graphene-cobalt interface have considered azimuthally-aligned lattices. Nonetheless, there is a range of possible commensurate structures with different azimuthal orientations between two nearly-matching hexagonal layers.[21] Indeed, chemical vapor deposition (CVD) growth of graphene on ultrathin Co films results in rotational disorder at the relatively low growth temperatures necessary to avoid film dewetting.[22–24] Considering all the research and applications centered around ultrathin films, it is important to understand the effect of rotational disorder by considering both structural and electronic aspects. Thus, we address here the existence of spin polarized bands near the Fermi level (also refereed to as the minicone state in the literature) in graphene with different rotational alignment with respect to the Co substrate.

In order to investigate the nature of the minicone state depending on the relative in-plane orientation between graphene and cobalt, we use CVD growth with ethylene as the precursor. The growth conditions are adjusted so that graphene domains with symmetry axe aligned or rotated with respect to those of the substrate form. By using spin- and energy-resolved two-dimensional (2D) momentum mapping, we show the presence of very similar electronic states near the Fermi level with linear band dispersion and high degree of spin polarization for both epitaxial and rotated graphene domains. The experimentally-observed properties of the minicone states are confirmed by density-functional theory (DFT) calculations taking into account the three most abundant graphene rotations at 19.2°, 22.4° and 16.5°. The theoretical calculations indicate that the $\overline{\mathrm{K}}$ points of commensurate Gr/Co superstructures coincide with that of the graphene primitive cell. Furthermore, DFT reveals a high degree of carbon character in the hybridized minicone states for all graphene rotations considered.

Results and discussion

Graphene was grown by ethylene CVD on a 50 ML (about 10 nm) Co film on W(110).[25] Growth at $p_{C2H4} = 1 \times 10^{-6}$ mbar and $T = 850$ K leads to the formation of various rotational domains of graphene consistently with the literature[22,24,26] (further details on sample growth and characterization can be found in Supplementary Material Section 1). Angle resolved photoemission and low-energy electron diffraction (LEED) patterns from the resulting surface featuring both rotated and epitaxial graphene domains are shown in Fig. 1a and 1b, respectively. In the 2D photoelectron momentum map in Fig. 1a obtained from the angle resolved photoemission spectroscopy (ARPES) measurement at constant binding energy near the Fermi level, the minicone feature reported in the literature can be discerned at the $\overline{\mathrm{K}}$ point of the epitaxial graphene domain (green arrow). In addition, a similar band feature is visible also at the respective $\overline{\mathrm{K}}$ points of the rotated graphene domains, as indicated by the red arrows. Based on this observation, we have studied the structural and electronic properties of different graphene domains in a comparative manner.

From the structural perspective, graphene azimuthal orientations and their relative abundance can be quantitatively obtained by measuring the intensity profile in the LEED pattern as seen in Fig. 1c along the path indicated in the inset. The azimuthal angle corresponding to the Co(0001) crystal vector is taken as the origin of the angular scale ϕ. By definition, epitaxial graphene domains appear at $\phi = 0$. The intensity profile reveals the presence of four broad diffraction peaks rather than a featureless diffraction ring expected from an entirely incoherent azimuthal distribution. The rotations are determined to be $\phi = 9.6°$, $16.5°$, $19.2°$, $22.4°$ by fitting the intensity profile with Gaussian peaks. The relative abundance of the $\phi \neq 0$ peaks are 4.7%, 38.2%, 40.6%, 16.5%, respectively. As it can be expected, these angles are close to some of the commensurate orientations found for two matching hexagonal lattices,[21] with small differences due to the strain between graphene and the cobalt support.

DFT calculations give further insight into the structural properties of the graphene/Co interface. We consider the three most represented rotated phases, in descending order of abundance: R19.2° (simulated as (8×8)R40.9° supercell), R16.5° (simulated as (7×7)R36.6° supercell), and R22.4° (simulated as $(\sqrt{7} \times \sqrt{7})$R40.9° supercell) (from here on, the experimentally determined rotation angle will be used to label the respective graphene domain), and compare their structural, energetic and electronic-structure properties to the ones of the epitaxially aligned graphene. The fully relaxed surface unit cell geometries are shown in Figs. 1d-g. The cohesive energy differences between the rotational phases and the epitaxial one are calculated to be all of the order of 100 meV per Co surface atom as can be seen in Table 1. Furthermore, the average graphene-Co distance, calculated as the difference between the average vertical position of C atoms and the average vertical position of top-layer Co atoms, is larger in the rotational phases as compared to the epitaxial one by 0.02-0.05 Å. The variations in the C positions for all graphene/Co phases are within 0.05 Å, which is significantly smaller than the typical buckling in graphene Moiré structures such as on Ru(0001) with about 1.5 Å buckling.[27] As for the isotropic tensile strain, R16.5° and R22.4° have the same value as in the epitaxial phase, while the strain is somewhat smaller in R19.2° (see Table 1).

The computed adsorption geometries consider rotational domains with almost fully relaxed graphene lattices. This is verified experimentally by LEED. The distance between the

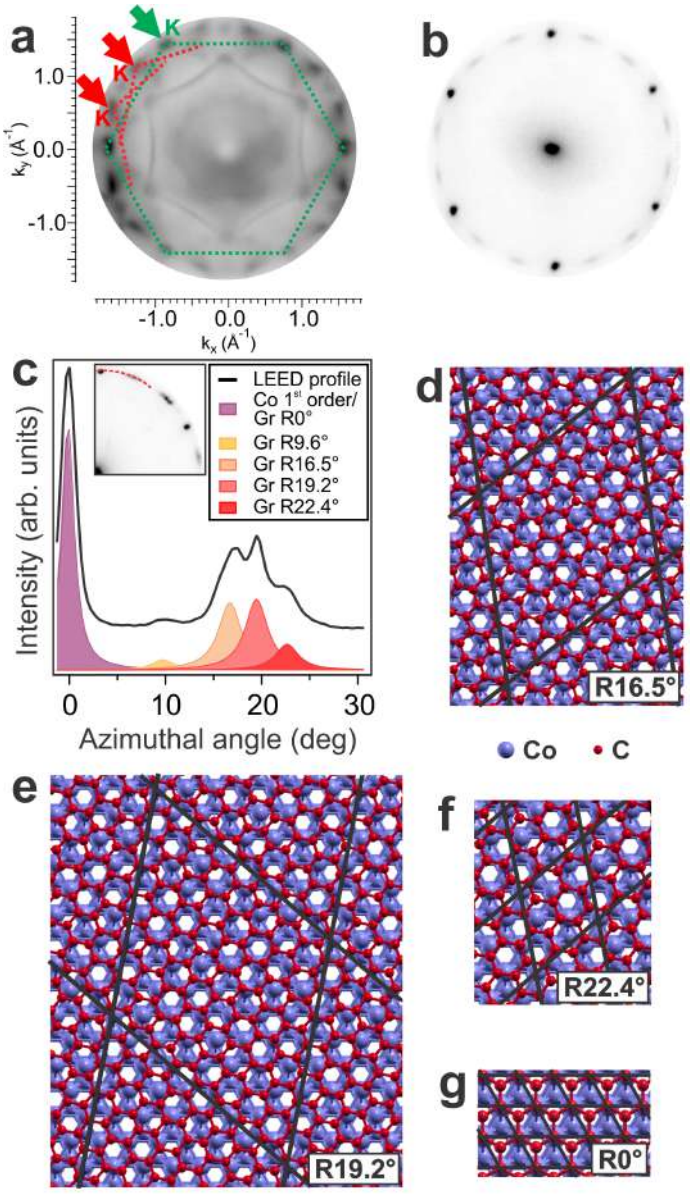

Figure 1: a) 2D momentum map near the Fermi level (E_b = 50 meV, $h\nu$ = 56 eV, p-polarisation, T = 130 K) of coexisting graphene domains with different azimuthal orientations, and b) the corresponding LEED pattern (V_{st} = 40 V). c) LEED intensity profile acquired along the curved path indicated in the inset. The intensity profile was fitted using Gaussian profiles. Optimized unit-cell geometries from DFT calculations for graphene orientations: d) R19.2°, e) R16.5°, f) R22.4°, g) epitaxial phase. The black lines denote the surface unit cell, while the red and blue circles represent the C and Co atoms, respectively, in (d-g).

Table 1: The cohesive energy (ΔE in eV per Co surface atom) relative to the epitaxial case, average distance between the Co surface and graphene ($\overline{d}$ in Å), and isotropic strain of graphene (ϵ in %) are shown for different rotational phases of graphene on Co(0001).

	R19.2°	R16.8°	R22.4°	epitaxial
ΔE	0.127	0.127	0.119	0.0
$\overline{d}$	2.13	2.12	2.10	2.08
ϵ	0.61	1.42	1.42	1.42

(00) and the first-order diffraction spots in $\phi \neq 0$ domains is $1.0 \pm 0.4\%$ larger with respect to that of $\phi = 0$ domains, consistently with the rotated domains relaxing towards the lattice constant of freestanding graphene.

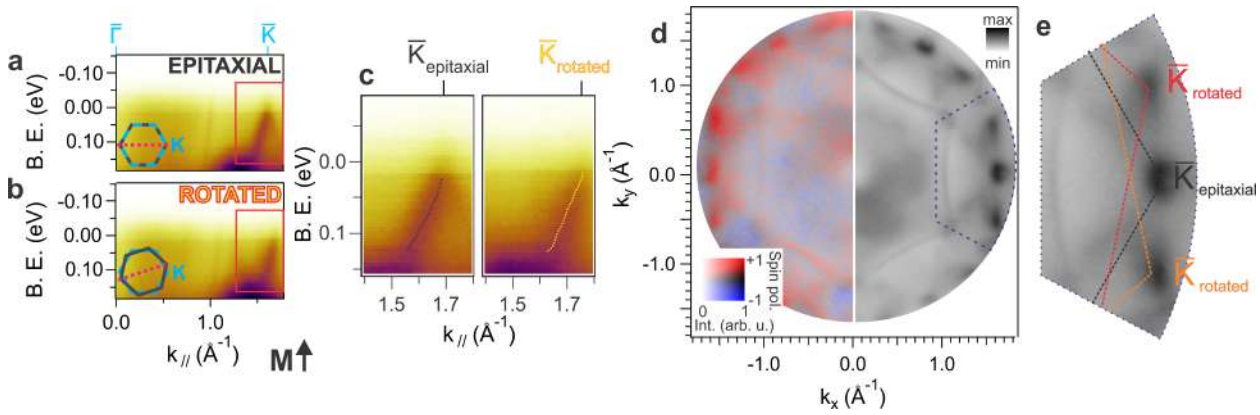

Figure 2: a) Energy-dependent ARPES intensity profile of epitaxial graphene acquired along the Co $\overline{\mathrm{K\Gamma K}}$ direction near Fermi level. b) Momentum map of rotated graphene acquired at 18° with respect to the Co $\overline{\mathrm{K\Gamma K}}$ direction. c) Comparison of the minicone bands for epitaxial and rotated graphene near their respective $\overline{\mathrm{K}}$ points, with the superimposed linearly dispersed MDC fitted maxima positions. d) Left: 2D spin resolved momentum map (E_B = 90 meV) of the sample composed by both epitaxial and rotated graphene domains; right: the corresponding spin integrated map. Zoom-in of the dashed region is shown in e). Dashed black, red and orange lines indicate the SBZs of the epitaxial, +18° and -18° rotated graphene, respectively. Prior to measurements, the sample was magnetized as shown on bottom of b) panel. All measurements were done at T_s = 130 K using $h\nu$ = 56 eV with p-polarization.

Electronic structures of the coexisting epitaxial and rotated graphene domains are compared in Fig. 2. Fig. 2a displays the energy-momentum map taken along the $\overline{\mathrm{K\Gamma K}}$ direction of Co(0001), which coincides with the $\overline{\mathrm{K\Gamma K'}}$ direction of the epitaxial graphene domains. The minicone state is seen at large momenta as an intense band with linear dispersion near E_F. The high intensity below about 0.15 eV binding energy corresponds to the Co *3d* states. Instead, Fig. 2b shows the energy-momentum map taken at an angle $\phi = 18°$ with respect to the $\overline{\mathrm{K\Gamma K}}$ direction of the Co(0001) substrate. Note that this angle corresponds to the weighted average of coexisting graphene rotational domains as found from the data displayed in Fig. 1c. We observe a pattern similar to the epitaxial orientation, characterized

by a linearly-dispersive band with the maximum at about 1.7 Å^{-1} away from $\overline{\Gamma}$ along the $k_{\parallel}$ direction. The maximum of the minicone state intersects the Fermi level at a slightly larger in-plane momentum transfer with respect to the epitaxial case (1.74 Å^{-1} *vs.* 1.70 Å^{-1}, respectively), as better appreciable in Fig. 2c. This is consistent with the structural relaxation of the rotated graphene domains observed in LEED. Note that the Co *3d* states appear with similar intensity in both the epitaxial and rotated profiles.

In order to determine the energy position of the minicone band apex in the case of rotated graphene we measured it with a high-resolution ARPES setup using s-polarized VUV photons as excitation source (see Supporting Information Fig. S4). By fitting the momentum map near the Fermi level of rotated graphene acquired along its $\overline{\Gamma K}$ direction (see Supporting Information Fig. S4), the apex of the minicone band is found at a binding energy of 25±15 meV, which is the same as that of epitaxial graphene. The lateral extent of the surface Brillouin zone (SBZ) is 1.9% larger in the case of rotated graphene with respect to the epitaxial case, in agreement with the LEED data. Moreover, the rotated minicone bands are broader in $k_{//}$ than their epitaxial counterpart, likely due to the presence of domains with slightly varying rotations all contributing to the same band feature. This augmented broadening can be observed in a 2D momentum map acquired close to the Fermi level (E_B = 90 meV), while the minicone bands from epitaxial graphene have a clear triangular shape (Fig. 2d), the minicone bands from rotated domains appear as elongated bands, aligned perpendicularly to the $\overline{\Gamma K}$ direction of Co(0001).

The Fermi velocity, derived from a linear fit to the measured energy dispersion of the minicone band, is found to be $v_F = 1.66 \times 10^5$ m/s for the epitaxial phase. In the case of rotated graphene, the corresponding value is $v_F = 1.95 \times 10^5$ m/s, which corresponds to an average over the rotated domains. On the other hand, the π band (main Dirac cone) apex of rotated phase is found at 2.45 eV with a band velocity of 0.95×10^6 m/s. Therefore, the rotated π band apex is shifted 0.38 eV towards lower binding energies in comparison to epitaxial graphene.[28] This is in line with a weaker graphene-cobalt interaction in the rotated graphene phase similarly to what has been observed in rotated graphene on Ni(111).[29]

As visible in Fig. 2d, upon graphene adsorption, the bands of the Co substrate maintain the same spin behavior as compared to the bare surface (see Supporting Information Fig. S5). In particular, minicone bands of epitaxial domains present a highly spin-polarized majority character (Fig. 2d), in line with previously reported results.[12,19,23,30,31] Using the procedure described in ref.,[32,33] the determined value of the spin polarization on the minicone in the epitaxial domains corresponds to 53±8%. Importantly, the minicone bands of rotated graphene present the same spin behavior as the epitaxial one. The measured value of spin polarization in the case of rotated graphene is 47±7%, which is comparable to the value of the epitaxial one. Note that the measured degree of spin-polarization can be underestimated due to the presence of magnetic domains as the measurement is done in remanence.

The nature and the origin of this linearly-dispersing spin-polarized state near Fermi level can be better understood by DFT calculations. Fig. 3 shows the calculated band structures along the $\overline{\Gamma K}$ direction for both majority and minority spins of R19.2°, and only majority spin of R16.5°, R22.4° and the epitaxial phase. Each band structure is unfolded from its respective supercell to the 1 × 1 graphene primitive cell.[34] Each of the phases possesses a minicone-like feature in the spin majority channel at the $\overline{K}$ point. By comparing majority and minority spin channels of R19.2° in Figs. 3a) and b), it can be concluded that

in our calculations the minicone is almost fully spin polarized (for the other phases, see Supplementary Information). Furthermore, the minicones of the rotated-graphene phases have a roughly similar appearance as the minicone of the epitaxial phase, but with a more pronounced linear dispersion.

The minicone bandgap opening in the rotated phases is of the order of a few meV as can be seen in Figs. 3(a-c), while the corresponding value for epitaxial graphene is 0.4 eV. In binding energy the minicone apex is found at 0.291 eV for $R19.2°$, 0.311 eV for $R22.4°$ and 0.267 eV for $R16.5°$, while in the epitaxial phase it is found at 0.302 eV binding energy, slightly higher compared to the two dominant rotated phases. All these values are about ~ 0.25 eV lower compared to the value found in the experiment. Similar or even larger shifts of the minicone between experiment and theory have been observed earlier for the DFT band structures of the epitaxial graphene/Co(0001) in generalized-gradient approximation .[35,36]

Estimated theoretical Fermi velocities of the minicone in the rotated phases at $\overline{\mathrm{K}}$ in the $\overline{\mathrm{K\Gamma}}$ direction vary from 2.3×10^5 m/s (R22.4°) to 2.6×10^5 m/s (R19.2°) and are significantly enhanced with respect to the estimated Fermi velocity of the epitaxial graphene (1.3×10^5 m/s). The increase of the Fermi velocity can be considered a further indication of a weaker substrate interaction in the rotated phase in comparison to the epitaxial graphene, as the stronger interactions due to the reduction of the graphene-Co distance are shown to flatten the minicone in the epitaxial graphene around the $\overline{\mathrm{K}}$ point. Note that the calculated band velocities compare reasonably well with the experimental values, confirming the correspondence between the experimentally-observed band feature and the calculated one.

Notably, orbital projections indicate a high degree of carbon orbital nature of the minicone states at $\overline{\mathrm{K}}$ (see Supporting information Fig. S6). In the majority spin channel carbon character of the minicone states in the rotated phases is estimated to be above 40-~~50~~%,[37] which is comparable to the calculated value of 55% for the epitaxial phase.

Furthermore, we also show the graphene primitive-cell character in Fig. 3 in color code, based on the spectral-weight calculation during the unfolding procedure,[34] which gives the probability that the eigenstate in the supercell has the same character as the primitive cell Bloch state to which it unfolds. The primitive character is a measure of the superlattice's modulation of the electronic structure with respect to the primitive cell. The unfolded minicone state at $\overline{\mathrm{K}}$ is trivially strongest in the epitaxial phase since the supercell coincides with the primitive cell. In the rotated phases, the primitive cell character is approximately 60%. In all the rotated phases considered, the states at $\overline{\mathrm{K}}$ of the graphene primitive cell are unfolded exclusively from the $\overline{\mathrm{K}}$ points of the superstructure unit cell. This results in the appearance of the minicones both at the primitive and supercell $\overline{\mathrm{K}}$ points and explains the observation that the minicone appears at the $\overline{\mathrm{K}}$ point of the primitive cell even in the rotated phases (Fig. 3f). Finally, the fact that the minicone has a more linear dispersion and is found at lower binding energy in the rotated phases relative to the epitaxial one is likely related to the specific strength of graphene-Co binding in the rotated phases. In the rotated phases, the binding is weaker than in the epitaxial phase, but the graphene-Co distances are still in the range of chemisorption distances and graphene appears without any rippling.

Conclusions

In this work, we demonstrate experimentally that epitaxial and rotated graphene domains host highly spin-polarized minicone features at the $\overline{\mathrm{K}}$ points of the respective graphene SBZ. The experimental findings are reproduced by DFT calculations performed for the four prevalent orientations of graphene on Co(0001). The calculations reveal a similar graphene character of the minicones in the rotated phases and the epitaxial phase. Furthermore, a smaller band-gap opening and a dispersion of the minicone closer to linear in the rotated phases, with respect to the epitaxial phase, have been found in the calculated band structures. In particular, an enhanced Fermi velocity of the minicone state with respect to the epitaxial graphene one has been observed both experimentally and theoretically. We find that all our experimental and theoretical findings originate from (i) the fact that the superstructure states at $\overline{\mathrm{K}}$, and thus the minicone states, unfold exclusively to the $\overline{\mathrm{K}}$ states in the primitive cell and (ii) the weaker graphene-Co binding in the rotational phases (due to the loss of C and Co orbital alignment) relative to the epitaxial phase, but which keeps some characteristics of chemisorbed graphene.

Considering the unavoidable presence of different rotational alignments of graphene grown especially on ultrathin Co films, our findings provide a solid experimental and theoretical basis for exploiting CVD synthesized graphene/Co(0001) interfaces in spintronics.

Methods

Surface Microscopy and Electron Diffraction

Spectroscopic PhotoEmission and Low-Energy Electron Microscope (SPELEEM, Elmitec) operating at the Nanospectroscopy beamline (Elettra synchrotron, Trieste)[38] was used for surface microscopy, microspot diffraction and spectroscopy measurements. In the SPELEEM setup, the sample is either illuminated with low-energy electrons (LEEM) or soft X-rays (XPEEM), giving structural and chemical information, respectively.[39,40] In LEEM, elastically backscattered electrons are directly imaged on a 2D detector through a system of electromagnetic lenses. The electron kinetic energy of the backscattered electrons is selected by tuning a voltage bias applied to the sample (start voltage, V_{st}). In addition to real space imaging, low-energy electron diffraction (LEED) patterns can be collected by imaging the backfocal plane of the objective lens. In diffraction mode operation, the probed area is limited to a micron sized region (μ-LEED) by using an area-selecting aperture. The lateral resolution in real space imaging is better than 10 nm in LEEM and 30 nm in XPEEM, whereas the transfer width in diffraction mode is below 0.05 $Å^{-1}$.[41]

Spin and Angle Resolved Photoemission Spectroscopy

Spin-resolved ARPES measurements were carried out using the NanoESCA photoemission microscope (PEEM) operating as a branchline at the Nanospectroscopy beamline. In the NanoESCA setup, the sample is illuminated with soft X-rays from the beamline equipped with two Apple-II type undulators. Photon energies cover a range from 40 eV to 1000 eV, and photon polarization can be set to linear horizontal, linear vertical or elliptical. The microscope, by properly tuning the electrostatic lenses, can operate in real space or reciprocal space mode (k-PEEM). The kinetic energy of the photoelectrons is selected by applying a proper bias voltage to the sample, similarly to the SPELEEM instrument. The photoemitted electrons are collected by an optical column, energy filtered in the double-hemispherical configuration (IDEA) and finally projected onto a 2D detector. In addition, spin-dependent reflectivity of a W(001) target inserted in the optical column allows to perform real or reciprocal space imaging with spin resolution.

Sample preparation

The W(110) crystal was cleaned by repeated annealing cycles to 1100°C in 3×10^{-7} mbar of molecular oxygen, followed by high temperature flashes in UHV up to 2000°C, until a sharp (1×1) LEED pattern was obtained. The temperature was measured using a C-type thermocouple in the SPELEEM, and a K-type in the NanoESCA setup. Cobalt was deposited using an e-beam evaporator, from a 99.995% purity Co rod, while keeping the sample at room temperature. A total of 50 ML Co was deposited at a rate of 2.3 Å/min. The evaporation rate was determined from the completion of the pseudomorphic layer on W(110). After deposition, the quality of the structure and cleanliness of the film was verified by LEED and XPS, respectively. The carbon for the graphene growth was provided by exposing the

surface to ethylene (C_2H_4) partial pressure of 5×10^{-7} mbar. The realignment of rotated graphene was performed by annealing the sample under UHV conditions up to 630 °C. In all the experiments the base pressure of the preparation and analysis chambers was below 2×10^{-10} mbar.

Theory

DFT calculations were performed in the plane-wave-pseudopotential approach, as implemented in the PWscf code, a part of the Quantum ESPRESSO distribution.[42] The generalized-gradient approximation for exchange and correlation in the Perdew–Burke–Ernzerhof parametrization and ultrasoft pseudopotentials are used. To account for van der Waals interactions, we applied the empirical DFT-D method.[43] The graphene-covered Co(0001) surfaces are simulated using the supercell method. The computational load due to the large lateral sizes of the rotated phases limited the thickness of the cobalt slab to three layers on top of which was an additional layer of graphene and a vacuum slab equivalent to 7 hexagonal-close packed (hcp) interlayer spacings. Our optimized bulk Co lattice constant is 2.501 Å with c/a ratio of 1.611, which is less than 0.7% smaller than the experimental values of 2.507 Å and c/a of 1.623.[44] For the epitaxial configuration, we used the fcc-top adsorption geometry.[24] The atomic positions are relaxed in the graphene and the interface Co layer, while the atomic positions in the bottom two Co layers are kept fixed at the bulk values. The $R22°$ phase which we simulated in our calculations can be denoted as $(\sqrt{7}\times\sqrt{7})R40.9°$ supercell. The primitive vectors spanning the unit cell of $R22°$ are rotated by 40.9° with respect to the Co $(10\bar{1}0)$-direction and the graphene is rotated by 21.7° relative to the Co $(10\bar{1}0)$-direction (and the epitaxial alignment) in $R22°$. In the $R19°$ phase, or $(8\times8)R40.9°$ supercell, the graphene is rotated by 19.1° with respect to the Co $(10\bar{1}0)$-direction. Finally, in the $R16°$ phase, denoted as $(7\times7)R36.6°$, graphene is rotated by 16.4° relative to the Co $(10\bar{1}0)$-direction.

A Monkhorst-Pack k-point mesh of $14\times14\times1$ centered at $\overline{\Gamma}$ is used for the epitaxial cell and scaled down for the supercells of the rotated graphene phases, so that the k-point density is kept constant. The wavefunction and density cutoff energies of 544 eV and 5442 eV are chosen, respectively. We employed a Gaussian level smearing of 0.136 eV. The forces were converged to better than 26 meV/Å.

Acknowledgement

References

(1) Fert, A.; Cros, V.; Sampaio, J. Skyrmions on the track. *Nature Nanotechnology* **2013**, *8*, 152–156.

(2) Zhan, Y.; Holmström, E.; Lizárraga, R.; Eriksson, O.; Liu, X.; Li, F.; Carlegrim, E.; Stafström, S.; Fahlman, M. Efficient Spin Injection Through Exchange Coupling at Organic Semiconductor/Ferromagnet Heterojunctions. *Advanced Materials* **2010**, *22*, 1626–1630.

(3) Wolf, S. A.; Awschalom, D. D.; Buhrman, R. A.; Daughton, J. M.; von Molnár, S.; Roukes, M. L.; Chtchelkanova, A. Y.; Treger, D. M. Spintronics: A Spin-Based Electronics Vision for the Future. *Science* **2001**, *294*, 1488–1495.

(4) Awschalom, D. D.; Flatté, M. E. Challenges for semiconductor spintronics. *Nature Physics* **2007**, *3*, 153–159.

(5) Han, Z.; Kimouche, A.; Kalita, D.; Allain, A.; Arjmandi-Tash, H.; Reserbat-Plantey, A.; Marty, L.; Pairis, S.; Reita, V.; Bendiab, N.; Coraux, J.; Bouchiat, V. Homogeneous Optical and Electronic Properties of Graphene Due to the Suppression of Multilayer Patches During CVD on Copper Foils. *Advanced Functional Materials* **2014**, *24*, 964–970.

(6) Soumyanarayanan, A.; Reyren, N.; Fert, A.; Panagopoulos, C. Emergent phenomena induced by spin–orbit coupling at surfaces and interfaces. *Nature* **2016**, *539*, 509–517.

(7) Wu, Q.; Shen, L.; Bai, Z.; Zeng, M.; Yang, M.; Huang, Z.; Feng, Y. P. Efficient Spin Injection into Graphene through a Tunnel Barrier: Overcoming the Spin-Conductance Mismatch. *Phys. Rev. Applied* **2014**, *2*, 044008.

(8) Dlubak, B.; Martin, M.-B.; Deranlot, C.; Servet, B.; Xavier, S.; Mattana, R.; Sprinkle, M.; Berger, C.; De Heer, W. A.; Petroff, F.; Anane, A.; Seneor, P.; Fert, A. Highly efficient spin transport in epitaxial graphene on SiC. *Nature Physics* **2012**, *8*, 557–561.

(9) Enoki, T.; Takai, K. The edge state of nanographene and the magnetism of the edge-state spins. *Solid State Communications* **2009**, *149*, 1144–1150.

(10) Yazyev, O. V.; Helm, L. Defect-induced magnetism in graphene. *Physical Review B* **2007**, *75*, 125408.

(11) Lehtinen, P. O.; Foster, A. S.; Ma, Y.; Krasheninnikov, A. V.; Nieminen, R. M. Irradiation-induced magnetism in graphite: a density functional study. *Physical review letters* **2004**, *93*, 187202.

(12) Dedkov, Y. S.; Fonin, M. Electronic and magnetic properties of the graphene–ferromagnet interface. *New Journal of Physics* **2010**, *12*, 125004.

(13) Decker, R.; Brede, J.; Atodiresei, N.; Caciuc, V.; Blügel, S.; Wiesendanger, R. Atomic-scale magnetism of cobalt-intercalated graphene. *Phys. Rev. B* **2013**, *87*, 041403.

(14) Pan, J.; Du, S.; Zhang, Y.; Pan, L.; Zhang, Y.; Gao, H.-J.; Pantelides, S. T. Ferromagnetism and perfect spin filtering in transition-metal-doped graphyne nanoribbons. *Phys. Rev. B* **2015**, *92*, 205429.

(15) Vu, A. D.; Coraux, J.; Chen, G.; N'Diaye, A. T.; Schmid, A. K.; Rougemaille, N. Unconventional Magnetisation Texture in Graphene/Cobalt Hybrids. *Scientific Reports* **2016**, *6*, 24783.

(16) Yang, H.; Chen, G.; Cotta, A. A. C.; N'Diaye, A. T.; Nikolaev, S. A.; Soares, E. A.; Macedo, W. A. A.; Liu, K.; Schmid, A. K.; Fert, A., et al. Significant Dzyaloshinskii–Moriya interaction at graphene–ferromagnet interfaces due to the Rashba effect. *Nature materials* **2018**, *17*, 605.

(17) Ajejas, F. et al. Unraveling Dzyaloshinskii-Moriya Interaction and Chiral Nature of Graphene/Cobalt Interface. *Nano Letters* **2018**, *18*, 5364–5372.

(18) Hallal, A.; Liang, J.; Ibrahim, F.; Yang, H.; Fert, A.; Chshiev, M. Rashba-Type Dzyaloshinskii–Moriya Interaction, Perpendicular Magnetic Anisotropy, and Skyrmion States at 2D Materials/Co Interfaces. *Nano Letters* **2021**, *21*, 7138–7144.

(19) Usachov, D.; Fedorov, A.; Otrokov, M. M.; Chikina, A.; Vilkov, O.; Petukhov, A.; Rybkin, A. G.; Koroteev, Y. M.; Chulkov, E. V.; Adamchuk, V. K.; Grüneis, A.; Laubschat, C.; Vyalikh, D. V. Observation of Single-Spin Dirac Fermions at the Graphene/Ferromagnet Interface. *Nano Letters* **2015**, *15*, 2396–2401.

(20) Günther, S.; Zeller, P. In *Encyclopedia of Interfacial Chemistry*; Wandelt, K., Ed.; Elsevier: Oxford, 2018; pp 295 – 307.

(21) Sboychakov, A. O.; Rakhmanov, A. L.; Rozhkov, A. V.; Nori, F. Electronic spectrum of twisted bilayer graphene. *Phys. Rev. B* **2015**, *92*, 075402.

(22) Mertins, H.-C.; Jansing, C.; Krivenkov, M.; Varykhalov, A.; Rader, O.; Wahab, H.; Timmers, H.; Gaupp, A.; Sokolov, A.; Tesch, M.; Oppeneer, P. M. Giant magneto-optical Faraday effect of graphene on Co in the soft x-ray range. *Phys. Rev. B* **2018**, *98*, 064408.

(23) Varykhalov, A.; Rader, O. Graphene Grown on Co(0001) Films and Islands: Electronic Structure and its Precise Magnetization Dependence. *Physical Review B* **2009**, *80*, 035437.

(24) Jugovac, M.; Genuzio, F.; Gonzalez, E. L.; Stojić, N.; Zamborlini, G.; Feyer, V.; Menteş, T. O.; Locatelli, A.; Schneider, C. M. Role of carbon dissolution and recondensation in graphene epitaxial alignment on cobalt. *Carbon* **2019**, *152*, 4.

(25) Jugovac, M. Morphology and electronic structure of graphene supported by metallic thin films. Dr., Universität Duisburg, Jülich, 2020; Universität Duisburg, Diss., 2020.

(26) Ago, H.; Ito, Y.; Mizuta, N.; Yoshida, K.; Hu, B.; Orofeo, C. M.; Tsuji, M.; ichi Ikeda, K.; Mizuno, S. Epitaxial Chemical Vapor Deposition Growth of Single-Layer Graphene over Cobalt Film Crystallized on Sapphire. *ACS Nano* **2010**, *4 12*, 7407–14.

(27) Wang, B.; Bocquet, M.-L.; Marchini, S.; Günther, S.; Wintterlin, J. Chemical origin of a graphene moiré overlayer on Ru(0001). *Phys. Chem. Chem. Phys.* **2008**, *10*, 3530–3534.

(28) Jugovac, M.; Genuzio, F.; Menteş, T. O.; Locatelli, A.; Zamborlini, G.; Feyer, V.; Schneider, C. M. Tunable coupling by means of oxygen intercalation and removal at the strongly interacting graphene/cobalt interface. *Carbon* **2020**, *163*, 341–347.

(29) Africh, C.; Cepek, C.; Patera, L. L.; Zamborlini, G.; Genoni, P.; Menteş, T. O.; Sala, A.; Locatelli, A.; Comelli, G. Switchable Graphene-Substrate Coupling Through Formation/Dissolution of an Intercalated Ni-Carbide Layer. *Scientific Reports* **2016**, *6*, 19734.

(30) Marchenko, D.; Varykhalov, A.; Sánchez-Barriga, J.; Rader, O.; Carbone, C.; Bihlmayer, G. Highly spin-polarized Dirac fermions at the graphene/Co interface. *Physical Review B* **2015**, *91*, 235431.

(31) Varykhalov, A.; Marchenko, D.; Sánchez-Barriga, J.; Scholz, M. R.; Verberck, B.; Trauzettel, B.; Wehling, T. O.; Carbone, C.; Rader, O. Intact Dirac Cones at Broken Sublattice Symmetry: Photoemission Study of Graphene on Ni and Co. *Physical Review X* **2012**, *2*, 041017.

(32) Tusche, C.; Ellguth, M.; Ünal, A. A.; Chiang, C.-T.; Winkelmann, A.; Krasyuk, A.; Hahn, M.; Schönhense, G.; Kirschner, J. Spin resolved photoelectron microscopy using a two-dimensional spin-polarizing electron mirror. *Applied Physics Letters* **2011**, *99*, 032505.

(33) Tusche, C.; Ellguth, M.; Krasyuk, A.; Winkelmann, A.; Kutnyakhov, D.; Lushchyk, P.; Medjanik, K.; Schönhense, G.; Kirschner, J. Quantitative spin polarization analysis in photoelectron emission microscopy with an imaging spin filter. *Ultramicroscopy* **2013**, *130*, 70–76.

(34) Medeiros, P. V.; Stafström, S.; Björk, J. Effects of extrinsic and intrinsic perturbations on the electronic structure of graphene: Retaining an effective primitive cell band structure by band unfolding. *Physical Review B* **2014**, *89*, 041407.

(35) Sipahi, G. M.; Žutić, I.; Atodiresei, N.; Kawakami, R. K.; Lazić, P. Spin polarization of Co(0001)/graphene junctions from first principles. *Journal of Physics: Condensed Matter* **2014**, *26*, 104204.

(36) Voloshina, E.; Dedkov, Y. In *Physics and Applications of Graphene: Experiments*; Mikhailov, S., Ed.; BoD – Books on Demand, 2011; Chapter 13.

(37) The calculated C-character in the rotational phases from the projection on the atomic orbitals is likely the lower limit considering that the atomic orbitals on which the projection is done are in the coordinate system defined by the Co atoms (and at angles of e.g. 19°, 16° and 22° with respect to the C-C bonds). This is not the case for the projection on atomic orbitals in the aligned phase.

(38) Locatelli, A.; Aballe, L.; Mentes, T. O.; Kiskinova, M.; Bauer, E. Photoemission Electron Microscopy with Chemical Sensitivity: SPELEEM Methods and Applications. *Surface and Interface Analysis* **2006**, *38*, 1554–1557.

(39) Locatelli, A.; Bauer, E. Recent Advances in Chemical and Magnetic Imaging of Surfaces and Interfaces by XPEEM. *Journal of Physics: Condensed Matter* **2008**, *20*, 093002.

(40) Bauer, E. *Surface microscopy with low energy electrons*; Springer, 2014; Vol. 23.

(41) Menteş, T. O.; Zamborlini, G.; Sala, A.; Locatelli, A. Cathode Lens Spectromicroscopy: Methodology and Applications. *Beilstein Journal of Nanotechnology* **2014**, *5*, 1873–1886.

(42) Giannozzi, P. QUANTUM ESPRESSO: a Modular and Open-Source Software Project for Quantum Simulations of Materials. *Journal of Physics: Condensed Matter* **2009**, *21*, 395502.

(43) Antony, J.; Grimme, S. Density functional theory including dispersion corrections for intermolecular interactions in a large benchmark set of biologically relevant molecules. *Physical Chemistry Chemical Physics* **2006**, *8*, 5287–5293.

(44) Taylor, A.; Floyd, R. W. Precision Measurements of Lattice Parameters of Non-Cubic Crystals. *Acta Crystallographica* **1950**, *3*, 285–289.

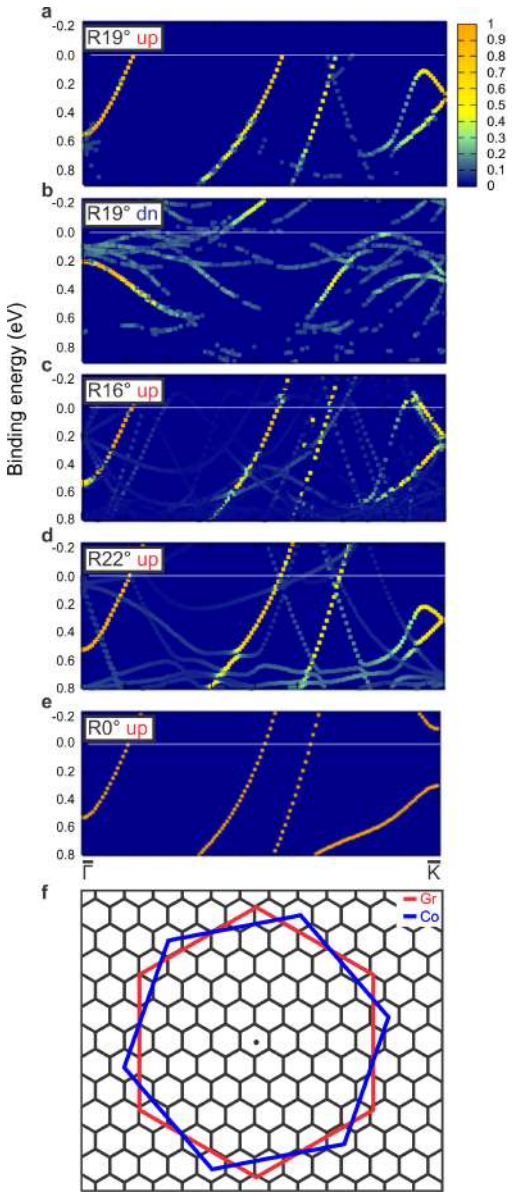

Figure 3: The calculated band structures for different rotated phases of graphene on Co(0001) unfolded into the 1×1 graphene primitive unit cell along $\overline{\Gamma\mathrm{K}}$ direction for a) majority and b) minority spin channels of $R19.2°$; majority spin channels of c) $R16.5°$, d) $R22.4°$ phase; d) the majority spin channel of the epitaxial graphene. The color bar indicates the strength of the primitive-cell character of the unfolded states. The unfolding has been performed using the BandUP code.[34] f) Brillouin zones of the graphene primitive cell (red), cobalt substrate (blue) and Gr/Co superstructure (black), shown for 19.2° Co *vs.* Gr azimuthal orientation. Note that the K points of the graphene primitive cell and the supercell coincide.